Structural identification of $Zn_xZr_yO_z$ catalysts for Cascade aldolization and self-deoxygenation reactions

Rebecca A.L. Baylon[a], Junming Sun[a,*], Libor Kovarik[b,c], Mark Engelhard[b,c], Houqian Li[a], Austin D. Winkelman[a], Yong Wang[a,b,*]

[a] *The Gene & Linda Voiland School of Chemical Engineering and Bioengineering, Washington State University, Pullman, WA 99164, USA*
[b] *Institute for Integrated Catalysis, Pacific Northwest National Laboratory, Richland, WA 99352, USA*
[c] *Environmental Molecular Sciences Laboratory, Pacific Northwest National Laboratory, Richland, WA 99352, USA*

ABSTRACT

Complementary characterizations, such as nitrogen sorption, X-ray diffraction (XRD), X-ray photoelectron spectroscopy (XPS), visible Raman, scanning transmission electron microscopy (STEM) coupled with elemental mapping, NH_3/CO_2 temperature programmed desorption (NH_3/CO_2-TPD), infrared spectroscopic analysis of adsorbed pyridine (Py-IR), and CO_2-IR, have been employed to identify the structure and surface chemistry (i.e., acid-base) of mixed $Zn_xZr_yO_z$ oxide catalysts of varied ratios of Zn/Zr. Atomically dispersed Zn^{2+} species are present in the framework within a thin surface shell (1.5–2.0 nm) of ZrO_2 particles when the Zn/Zr ratio is smaller than 1/10; when the ratio is above this, both atomically dispersed Zn^{2+} and ZnO clusters coexist in mixed $Zn_xZr_yO_z$ oxide catalysts. The presence of ZnO clusters shows no significant side effect but only a slight increase of selectivity to CO_2, caused by steam reforming. The incorporation of atomic Zn^{2+} into the ZrO_2 framework was found to not only passivate strong Lewis acid sites (i.e., Zr-O-Zr) on ZrO_2, but to also generate new Lewis acid-base site pairs with enhanced Lewis basicity on the bridged O (i.e., $Zr\!-\!\overset{\frown}{O}\!-\!Zn$). In the mixed ketone (i.e., acetone and methyl ethyl ketone (MEK)) reactions, while the passivation of strong acid sites can be correlated to the inhibition of side reactions, such as ketone decomposition and coking, the new Lewis acid-base pairs introduced enhance the cascade aldolization and self-deoxygenation reactions involved in olefin ($C_3^=$-$C_6^=$) production. More importantly, the surface acid-base properties change with varying Zn/Zr ratios, which in turn affect the cross- and self-condensation reactivity and subsequent distribution of olefins.

$$Zr\!-\!\overset{\frown{e}}{O}\!-\!Zn$$
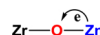
1. Introduction

Global demand for olefins is increasing continuously [1,2]. The primary use for lower olefins, such as propylene and butylene, are as chemical feedstocks [3,4]. For example, propylene is used as a building block for chemicals including polypropylene, propylene oxide, and acrylonitrile. Four-carbon olefins (e.g., 1-butene, 2-butene, isobutene) are of interest due to their use in the production of methyl tert-butyl ether (MTBE) and ethyl tert-butyl ether (ETBE) [5]. Five-carbon and C_6 olefins can be blended to form gasoline, alkylated with isobutene to form higher fuel range hydrocarbons, or used as starting material in polymers, fatty acids, mercaptans, and surfactants [6,7]. Traditionally, the primary source of three and four-carbon olefin production has been

from non-renewable fossil fuel resources via naphtha steam cracking. However, there has been much recent interest in finding renewable methods of olefin production due to the concern of diminishing fossil fuel resources [8,9].

Biomass is widely recognized as a primary renewable energy source [10–12]. For lignocellulosic biomass, conversion to hydrocarbons typically is carried out as a multi-step process. One typical example is fast pyrolysis of biomass to yield pyrolysis oil, or bio-oil. This bio-oil is then further converted to hydrocarbon fuels through hydrotreating processes albeit the low carbon yield [11–13]. Significant amounts of small oxygenates like alcohols, carboxylic acids, and ketones can also be derived via pyrolysis of lignocelluosic biomass [12,14]. On the other hand, biomass can also be readily converted to ethanol and acetic acid

through commercially viable processes, such as fermentation [15]. It can be anticipated that the biomass-derived small oxygenates will be abundant in the near future. With increased availability and decreased cost, achieving effectual catalytic conversion of those small oxygenates (e.g., carboxylic acids, alcohols and ketones) to valuable chemicals like C_3-C_6 olefins is essential to move away from our current dependence on non-renewable fossil resources and finding a renewable and sustainable means to their production.

A crucial step in converting biomass derived components to fuels and chemicals is oxygen removal. Additionally, control over C−C bond formation is necessary to provide the desired hydrocarbon chain length of products [16–20]. Various heterogeneous catalysts have been investigated to convert small oxygenates (e.g., alcohols, ketones, and carboxylic acids) to olefins [21–27]. Direct ethanol dehydration to ethylene has been extensively studied, and advances in this area have been summarized recently [21]. Zeolites (e.g., HZSM-5, LEV zeolite, HSAPO) have been successful in converting small oxygenates commonly found in bio-oil to a mixture of olefins and aromatics [23,28–32]. Their disadvantages include low activity, hard-to-control selectivity between olefins and aromatics, and coke generation that inhibits catalytic activity [23,33]. Conversion of ethanol to propylene has also been reported via a proposed dehydration, polymerization and cracking mechanism over LEV zeolites. These catalysts show both low selectivity and low stability due to fast coking reactions [34,35]. Recently, Iwamoto and coworkers developed a new strategy to selectively convert ethanol to propylene using catalysts such as Ni-M41, Sc/In$_2$O$_3$, and Y$_2$O$_3$-CeO$_2$ [22]. The reaction pathway was found to involve ethanol dehydrogenation to acetaldehyde followed by a condensation or ketonization reaction to acetone. The acetone intermediate is then hydrogenated to isopropyl alcohol followed by dehydration that results in a higher selectivity to propylene than what is achievable on traditional zeolite catalysts. For converting carboxylic acids to chemicals ketonization, a bimolecular reaction in which two carboxylic acids couple to form a ketone, is generally used. In this particular case, not only does this reaction achieve C−C coupling to increase the chain-length of the resulting ketone, but ketonization can accomplish oxygen removal, leading to only CO_2 and H_2O as byproducts. This reaction has been well studied over alkaline-earth-metal oxides and transition-metal oxides such as Mn$_2$O$_3$–CeO$_2$, ZrO$_2$, and TiO$_2$ [36–38]. A variety of proposed reaction mechanisms exist for this reaction over different metal oxides [39]. In separate works, ketone to olefin conversion has been reported over zeolites, where Brønsted acid sites are considered to be the active sites involved in the reaction, as well as over transition-metal oxides [40–46].

We have recently developed unique $Zn_xZr_yO_z$ mixed-metal oxide catalysts for a cascade ethanol-to-isobutene (ETIB) reaction [47–49]. The $Zn_xZr_yO_z$ mixed-metal oxide catalyst was later found by other groups for direct acetic acid-to-isobutene conversion [50], for upgrading of syngas-derived small oxygenates to produce olefins [51,52], and for catalyzing low-temperature ethanol dehydrogenation reactions [53]. Our recent work into this catalyst revealed that, when compared with Brønsted acid sites, Lewis acid-base site pairs are more durable and selective for the cascade ETIB reaction, especially for acetone-to-isobutene conversion (the rate determining step of the cascade reaction) [47]. Moreover, the mixed-metal oxide catalyst $Zn_1Zr_{10}O_z$ (i.e. possessing a Zn/Zr ratio of 1/10) is also highly active and stable for cascade self- and cross-ketonization, self- and cross-aldolization, and deoxygenation reactions for converting mixed carboxylic acids (e.g., mixed acetic acid and propanonic acid) into C_3-C_6 olefins [25,54,55]. More recent work by other groups also suggests that the redox properties of mixed-metal oxides could play key roles in some of the elementary steps of the cascade ETIB reactions (e.g., dehydrogenation and ketonization) [56,57]. It should be noted that despite insight gained in the above-mentioned studies on $Zn_xZr_yO_z$ mixed-metal oxide catalysts, the specific Zn^{2+} structure (i.e., Zn^{2+} location and degree of dispersion) and its effect on the surface chemistry (e.g., Lewis acid-base properties) of the catalyst remain unclear, and whether this surface chemistry affects the cross-condensation of the mixed acid feed is yet to be explored. Through this work, by using complimentary characterizations such as nitrogen sorption, XRD, XPS, visible Raman, STEM, NH$_3$-TPD, CO$_2$-TPD, Py-IR, and CO$_2$-IR, we have further identified the surface structure and functionality of $Zn_xZr_yO_z$ mixed-metal oxide catalysts with varied Zn/Zr ratios. In particular, we report findings on the structure of Zn^{2+} species and its effect on the acid-base properties of the catalyst surface. The rate-determining mixed ketone reactions (acetone and methyl ethyl ketone), for simplicity, were mainly used to investigate how the surface acid-base properties affect the self- and cross-aldolization and self-deoxygenation of ketones, which effectively control the product distribution of C_3-C_6 olefins.

2. Experimental

2.1. Materials and catalyst synthesis

Zr(OH)$_4$ (MEL, XZO631/01), Zn(NO$_3$)$_2$·6H$_2$O (Sigma-Aldrich, reagent grade, 98%), ZnO powder (Sigma Aldrich), Methyl ethyl ketone (MEK, 99.7%), Acetone (J.T. Baker, 99.8%), Pyridine (J.T. Baker, 100%). The $Zn_xZr_yO_z$ catalysts (x, y, and y represent the molar ratio of each component) were synthesized via incipient wetness impregnation using Zr(OH)$_4$ (MEL, XZO631/01) as the support. Briefly, the Zr(OH)$_4$ powder was dried at 105 °C overnight before impregnation with Zn(NO$_3$)$_2$·6H$_2$O (Sigma-Aldrich, reagent grade, 98%) precursor solution. The concentration of the solution was adjusted to achieve the desired Zn/Zr ratio. After drying this mixture at room temperature overnight and then at 105 °C for 4 h, it was then heated to 400 °C at 3 °C/min and calcined at this temperature for 2 h. The samples were then heated to 550 °C at 5 °C/min and calcined at this temperature for 3 h. ZrO$_2$ samples were prepared via calcination of Zr(OH)$_4$ in air following the same calcination procedure described above.

2.2. Characterization

Specific surface areas of the catalysts were determined via nitrogen sorption experiments carried out on a Micromeretics TriStar 2 3020 physisorption analyzer. Catalyst samples were degassed at 350 °C for 3 h under vacuum before experiments were carried out at a temperature of −196 °C.

The bulk phases of the $Zn_xZr_yO_z$ samples were analyzed by X-ray diffraction. The diffractograms were recorded on a Rigaku Miniflex 600 apparatus using Ni-filtered Cu Kα radiation (λ = 0.15406 nm). For each sample, Bragg's angles between 10° and 90° were scanned at a rate of 1.4°/min.

XPS measurements were performed with a Physical Electronics Quantera Scanning X-ray Microprobe. This system uses a focused monochromatic Al Kα X-ray (1486.7 eV) source for excitation and a spherical section analyzer. The instrument has a 32 element multichannel detection system. The X-ray beam is incident normal to the sample and the photoelectron detector is at 45° off-normal. High energy resolution spectra were collected using a pass-energy of 69.0 eV with a step size of 0.125 eV. For the Ag 3d$_{5/2}$ line, these conditions produced a FWHM of 1.0 eV ± 0.05 eV. The binding energy (BE) scale was calibrated using the Cu 2p$_{3/2}$ feature at 932.62 ± 0.05 eV and Au 4f$_{7/2}$ at 83.96 ± 0.05 eV. Low energy electrons at 1 eV and 20 μA, and low energy Ar$^+$ ions were used to minimize the charging effect on the samples analyzed. Quantification was performed using standard sensitivity factors contained in the ULVAC-PHI, Inc. MultiPak software V9.6.1.7 dated October 2016. Peak area intensities required for quantification were calculated after applying Shirley background subtraction to the data. These quantification results include the instrument transmission function, source angle, and asymmetry corrections.

Transmission electron microscopy (TEM) imaging was performed on a FEI Titan 80–300 operated at 300 kV. The images were acquired with

a High Angle Annular Dark Field Detector (HAADF) in Scanning Transmission Electron mode. The semi-convergence angle was set to 17.8 mrad, and the inner collection angle was set above 54 mrad. Compositional analysis was performed with a JEOL ARM 200 operated at 200 kV. The microscope houses a high-collection angle Silicon Drift Detector SDD (100 mm^2). The samples were prepared by dispersing a dry powder on a lacey-carbon coated 200 mesh Cu grids.

Raman spectra were taken on a Horiba LabRAM HR Raman spectrometer with a Ventus LP 532 nm laser. Prior to the Raman measurements, the sample was pretreated in a Linkam CCR1000 in situ cell heated to 450 °C at a temperature ramp rate of 10 °C/min for 1 h before allowing the sample to cool to room temperature under a 50 sccm flow of N$_2$. Spectra were recorded at room temperature.

Infrared spectroscopic analysis of adsorbed pyridine (Py-IR), CO$_2$ (CO$_2$-IR), and hydroxyl groups were recorded using a Bruker Tensor 27 FTIR spectrometer. For Py-IR and CO$_2$-IR, about 20 mg of the catalyst was loaded into an *in situ* cell that was then pretreated at 450 °C for 1 h in He at a flowrate of 50 sccm. After the sample was allowed to cool to 50 °C, a background spectra was taken. The corresponding probe molecule was then introduced to the cell via a bubbler using He at a flowrate of 10 sccm or 25 vol % CO$_2$/Ar at a flowrate of 10 sccm as the gas carrier for around 10 min until IR spectra from continuous scans indicated saturation of the probe molecule on the surface of the catalyst. Physisorbed species were removed by flowing He at 50 sccm over the catalyst for 30 min at 50 °C. The sample was heated to the desired desorption temperature at a temperature ramp rate of 10 °C/min and scans were taken for 30 min. The sample was then allowed to cool to 50 °C and scanned for the generation of difference spectra presented in this report. For IR analysis of the surface hydroxyl groups, KBr was used to acquire the background spectra. The same procedure was followed for acquiring the difference spectra of the hydroxyl groups on the catalyst surface sans probe molecule adsorption.

NH$_3$ and CO$_2$ temperature programmed desorption (NH$_3$-TPD, CO$_2$-TPD) were carried out using a Micromeritics Autochem 2920 equipped with a ThermoStar TM GSD 320 mass spectrometer. One-hundred milligrams of the catalyst was loaded and pretreated by heating to 450 °C at a temperature ramp rate of 10 °C/min where it was held at this temperature for 30 min under 50 sccm He flow. The sample was then allowed to cool to 50 °C and the probe molecule (NH$_3$ or CO$_2$) was then allowed to flow over the sample until saturation was observed from the IR spectra measurements. Fifty standard cubic centimeters of 5% Ar in He was flowed to remove any physisorbed species on the catalyst surface. The sample was then heated to 600 °C at a temperature ramp rate of 20 °C/min and the composition of effluent gas was monitored using the mass spectrometer. A 5 mol % Ar tracer in He was used as a reference gas, and the relative response factors calibrated for NH$_3$ (R_{NH3}/R_{Ar}) and CO$_2$ (R_{CO2}/R_{Ar}) were used to quantify the amount of NH$_3$ and CO$_2$ that desorbed from the surface of the catalyst.

2.3. Catalytic activity testing

Catalytic activities were evaluated by a test unit built in-house described in previous work [24,47]. Catalyst samples were loaded into a stainless steel tubular fixed-bed reactor (I.D. 4 mm) where it then was pretreated at 450 °C under 50 sccm nitrogen flow for 30 min. A steam to carbon (S/C) ratio of 5 was used. Feed solution was introduced into the reactor with an evaporator kept at 150 °C and N$_2$ flow as a carrier gas. An online Shimadzu GC-2014 Gas Chromatograph (GC) analyzed products via an auto sampling valve which sent effluent through an HP-Plot Q column (30 m, 0.53 mm, 40 um) to a flame ionization detector (FID) and a thermal conductivity detector (TCD) inside the unit.

Conversion (X_r) and product carbon selectivity ($S_{products-i}$) were calculated as follows: $X_r = (mol_{reactant-in} - mol_{reactant-out})/mol_{reactant-in}$; $S_{products-i} = (mol_{product-i} \times \alpha_i)/(mol_{reacted\ reactant} \times \beta)$, where α_i and β refers to the carbon number in product-i and reactant, respectively. Carbon yield was calculated as follows: $X_r \times S_{products-i}$.

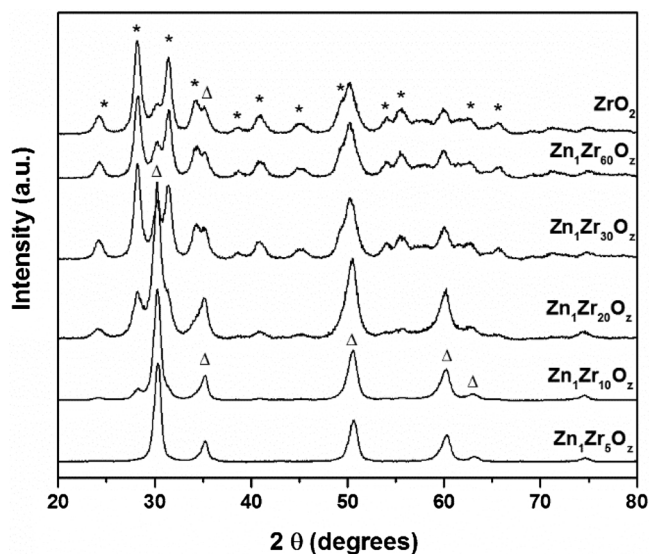**Fig. 1.** XRD patterns of ZrO$_2$ and Zn$_x$Zr$_y$O$_z$ catalysts (with varying catalyst Zn/Zr ratios of 1/60-1/5). The triangle denotes peaks unique to the tetragonal phase and stars denote those unique to the monoclinic phase.

3. Results

3.1. Characterization of Zn$_x$Zr$_y$O$_z$ catalyst

3.1.1. Structure identification of Zn$_x$Zr$_y$O$_z$ catalyst

BET surface areas of Zn$_x$Zr$_y$O$_z$ were measured using N$_2$ sorption. When the Zn/Zr ratio was increased from 0 to 1/5, the surface area slightly decreased from 75 m^2/g to 70 m^2/g. This suggests that Zn/Zr ratios studied in this work barely influence the porosities of the Zn$_x$Zr$_y$O$_z$ catalysts.

XRD patterns of bulk ZrO$_2$ and Zn$_x$Zr$_y$O$_z$ catalysts are shown in Fig. 1. Over ZrO$_2$, the main peaks at 24.2, 28.2, 31.4, 34.2, 38.5, 40.8, 45.0, 49.5, 54.2, 55.8, 62.8, 66.8, and 72.0° indicate that bulk ZrO$_2$ predominantly has the monoclinic phase (i.e., m-ZrO$_2$) [58]. The minor or shoulder peaks at 30.4, 35.2, 50.2, and 59.8° are assigned, with further confirmation later through Raman spectral data, to the tetragonal phase of ZrO$_2$ (t-ZrO$_2$) [59]. It was observed that upon increasing the loading of ZnO (increasing Zn/Zr molar ratio) in the mixed-metal catalysts, the fraction of tetragonal phase ZrO$_2$ increases. This conclusion was reached from observation that as Zn was added to the catalyst the peaks corresponding to m-ZrO$_2$ decreased in intensity, while peaks characteristic of the t-ZrO$_2$ phase intensified. When the Zn/Zr ratio is higher than 1/20, t-ZrO$_2$ begins to dominate, and peaks characteristic of the monoclinic phase decrease in intensity until fully disappearing at a ratio of Zn/Zr = 1/5. This observation suggests that Zn addition facilitates the formation of tetragonal phase ZrO$_2$ on Zn$_x$Zr$_y$O$_z$ catalysts [60,61]. Additionally, no ZnO diffraction is observed in any of the XRD spectra studied, suggesting a high level of dispersion of ZnO on the Zn$_x$Zr$_y$O$_z$ catalysts.

Given their similar lattice parameters, the exclusive use of XRD spectra to assign observed peaks to tetragonal and cubic ZrO$_2$ phases could potentially be misleading. Because of this, complementary Raman spectra of the catalysts (Fig. 2) were taken to further understand their structure. The peaks associated with t-ZrO$_2$ (312, 269, 149 cm^{-1}) and m-ZrO$_2$ (634, 616, 556, 472, 377, 181 cm^{-1}) were detected on all the catalysts studied [62,63]. The data show that the fraction of t-ZrO$_2$ increases—as the fraction of m-ZrO$_2$ decreases—with increasing Zn/Zr ratios, which is consistent with the XRD results. In contrast to XRD observations, tetragonal peaks appear only after Zn/Zr = 1/10 and become dominant at Zn/Zr = 1/5 in the Raman spectra. Although UV Raman spectroscopy (244 nm) is classified as a surface technique, the
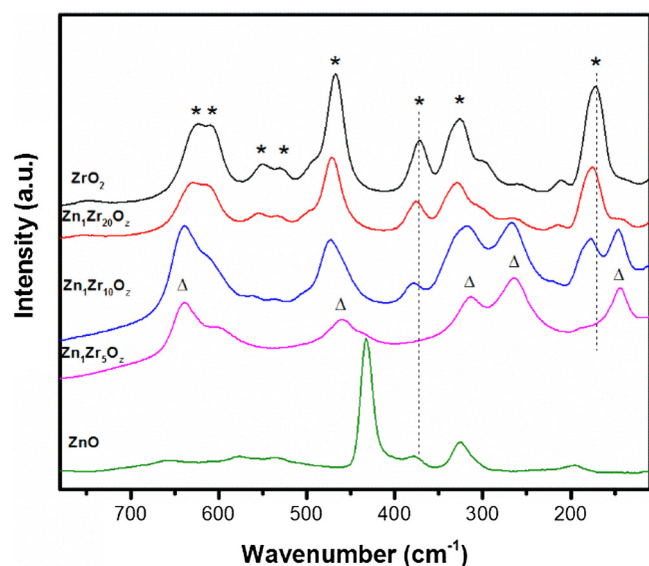
Fig. 2. Raman spectra of ZnO, ZrO$_2$ and Zn$_x$Zr$_y$O$_z$ catalysts (Zn/Zr = 1/20-1/5). The triangle denotes peaks unique to the tetragonal phase and stars denote those unique to the monoclinic phase.

visible laser (532 nm) used for the Raman analyses here has been reported to show information for both the bulk and some of the surface of the sample [63]. The latter contradictory observation suggests that visible Raman is likely picking up structural information near or at the surface of the catalyst, while the XRD detector does not, suggesting that the surface phase of Zn$_x$Zr$_y$O$_z$ is enriched with m-ZrO$_2$ and that its depth or domain size varies with Zn addition. More importantly, given the surface monoclinic structure, its band position (e.g., the peak at ~ 181 cm^{-1} and ~ 372 cm^{-1}) blue-shifts as Zn^{2+} content increases (Fig. 2), which is an indication of shortening Zr–O bonds of m-ZrO$_2$ with increasing Zn^{2+} content [63,64]. This suggests that Zn^{2+} is either incorporated into the bulk ZrO$_2$ lattice [60,62,63] or chemically bonded on the ZrO$_2$ to form surface Zr-O-Zn moieties (both are defined as framework Zn^{2+} in this paper). Given the easy access nature, the surface Zr-O-Zn is believed to be essential to the unique catalytic properties of Zn$_x$Zr$_y$O$_z$ that will be further discussed in the following sections. In addition, ZnO (zincite) is not detected by Raman until the content of Zn reaches Zn/Zr = 1/5, where a shoulder peak at ~ 432 cm^{-1} can be distinguished.

To further confirm these results, HAADF STEM imaging combined with elemental mapping (Fig. 3) was used to study the structure of Zn$_1$Zr$_5$O$_z$ and Zn$_1$Zr$_{10}$O$_z$. Over Zn$_1$Zr$_{10}$O$_z$, t-ZrO$_2$ was found to be the dominant phase present. However, surface m-ZrO$_2$ domains were clearly identified, and coexist by sharing the same epitaxial (001) with t-ZrO$_2$ (Fig. 3A). No m-ZrO$_2$ was identified by STEM on the Zn$_1$Zr$_5$O$_z$ catalyst (Fig. 3C). Elemental mapping analysis was also used to carefully analyze different particles of the two samples (Figs. S1 and S2). In general, zinc was found to be evenly dispersed on the Zn$_1$Zr$_{10}$O$_z$ catalyst (Fig. 3B), while enriched ZnO clusters were clearly identified on the Zn$_1$Zr$_5$O$_z$ catalyst (Fig. 3D). These results are in agreement with the observations made from Raman spectra.

The distinct IR patterns of surface hydroxyl groups between that of t-ZrO$_2$ and m-ZrO$_2$ [65] were used as fingerprints to identify the surface m-ZrO$_2$ phase on Zn$_1$Zr$_{10}$O$_z$ [47]. Separate IR experiments were also performed in order to study the hydroxyl groups on the Zn$_x$Zr$_y$O$_z$ catalysts (Fig. 4). Surprisingly, even the Zn$_1$Zr$_5$O$_z$ catalyst, on which no m-ZrO$_2$ was detected by either Raman and STEM, IR still shows the hydroxyl group fingerprint indicative of the monoclinic ZrO$_2$ phase (i.e., dominant peaks at 3676 and 3770 cm^{-1}) rather than the tetragonal one (i.e., dominant peak 3735 cm^{-1}) on the surface [65]. It is worth mentioning that a shoulder peak at 3700 cm^{-1} (hydroxyl groups in

proximity to oxygen vacancy [66]) increases as Zn content in the catalyst increases. These results, as proposed by Li et al. on a heteroatom (i.e. Y)-doped ZrO$_2$ [63], suggest that the surface of the Zn$_x$Zr$_y$O$_z$ could feature a thin layer of monoclinic ZrO$_2$ phase structure after thermal treatment (i.e., calcination), whereas, the bulk tetragonal ZrO$_2$ phase is stabilized due to the introduction of oxygen vacancies [61]. As Zn content increases, the monoclinic phase layer becomes thinner or changes into very small domains that are beyond the detection limit of techniques such as XRD, Raman, and STEM, but is still differentiable from hydroxyl group pattern in IR spectra.

XPS analysis was also performed to investigate the surface chemistry of the Zn$_x$Zr$_y$O$_z$ catalysts. To measure uniformity of Zn distribution, two spots on each sample were scanned. A quantitative analysis of surface elements is summarized in Table S1, which shows that the Zn species are indeed uniformly distributed on the catalysts. Fig. 5 presents the representative Zn 2p and O 1 s XPS spectra of the catalysts. Due to the extremely low level of carbon on most of the catalysts, all the spectra are referenced to Zr 3d$_{5/2}$ at 182.2 eV. We surmise that the perturbation of incorporated Zn^{2+} on electronic properties of Zr is minimal since the atoms are separated by one lattice/bridged oxygen. Over Zn$_1$Zr$_{60}$O$_z$, a binding energy of 1022.1 eV is observed, an upper shift of 0.4 eV relative to that of ZnO. This suggests that the Zn^{2+} in Zn$_1$Zr$_{60}$O$_z$ is more electron deficient, further confirming that Zn^{2+} is incorporated in the framework of ZrO$_2$. As the Zn/Zr ratio in the catalyst increases, the binding energy shifts monotonically to lower energy levels and eventually approaches that of ZnO at 1021.7 eV. This upshift of binding energy was also observed on hard-template derived Zn$_x$Zr$_y$O$_z$ catalysts by Wang et al. [53]. On the other hand, the incorporation of Zn^{2+} into the ZrO$_2$ framework also affects the electronic properties of lattice oxygen, shifting the binding energy of O1s slightly from 530.1 eV on ZrO$_2$ to 529.9 eV on Zn$_1$Zr$_5$O$_z$. The shift to lower binding energy of O 1 s when framework Zn^{2+} is present suggests that the incorporated Zn^{2+} donates part of its electrons to the bridged oxygen to which it is bonded. The donation of part of the electrons from Zn^{2+} to neighboring bridged oxygen atoms could contribute to the enhanced surface basicity of the bridge oxygen on the Zn$_x$Zr$_y$O$_z$ catalysts (i.e., Zr—O—Zn), which will be further discussed in the following discussions on the acid-base properties of these catalysts. Other than the electronic properties, it was also observed that the measured surface Zn/Zr molar ratio is always more than two times higher than the ideal bulk Zn/Zr molar ratio (Table 1), but an order of magnitude lower than the hypothetical surface Zn/Zr ratio (calculated based on the assumption that all the added Zn^{2+} stays on the outer surface of the Zn$_x$Zr$_y$O$_z$ particles). This observation suggests that most of Zn^{2+} species are enriched on the outer surface of the Zn$_x$Zr$_y$O$_z$ catalyst particles. Given the uniform distribution of Zn^{2+} on the surface, if we assume the distribution of Zn^{2+} is uniform with depth, then the calculated shell thickness where Zn^{2+} are located is 1.5-2.0 nm (Table 1). Note that the real distribution of subsurface Zn^{2+} is subject to further systematic investigations using low energy sputtering combined with XPS analysis.

In summary, based on complimentary characterization methods, only atomically dispersed Zn^{2+} is present in framework of a thin outer layer of 1.5–2.0 nm thickness in the Zn$_x$Zr$_y$O$_z$ catalyst particles when the Zn/Zr ratio is less than 1/10. When the Zn/Zr ratio is above 1/10 other than the framework Zn^{2+}, ZnO clusters appear and co-exist on the outer surface of the catalysts. While the incorporation of Zn^{2+} also causes the stabilization of t-ZrO$_2$ bulk phase, the surface chemistry of the Zn$_x$Zr$_y$O$_z$ seems identical to that of monoclinic one, evidenced by IR spectra of hydroxyl groups. Most importantly, the incorporation of atomically dispersed Zn^{2+} generates new surface Lewis acid-base site pair (i.e., Zr—O—Zn) of different electronic properties from both ZnO and ZrO$_2$.

3.1.2. Acid-base properties

Our previous Py-IR experiments on ZrO$_2$ and Zn$_1$Zr$_{10}$O$_z$ [47] showed that bulk ZrO$_2$ contains predominantly Lewis acid sites with a

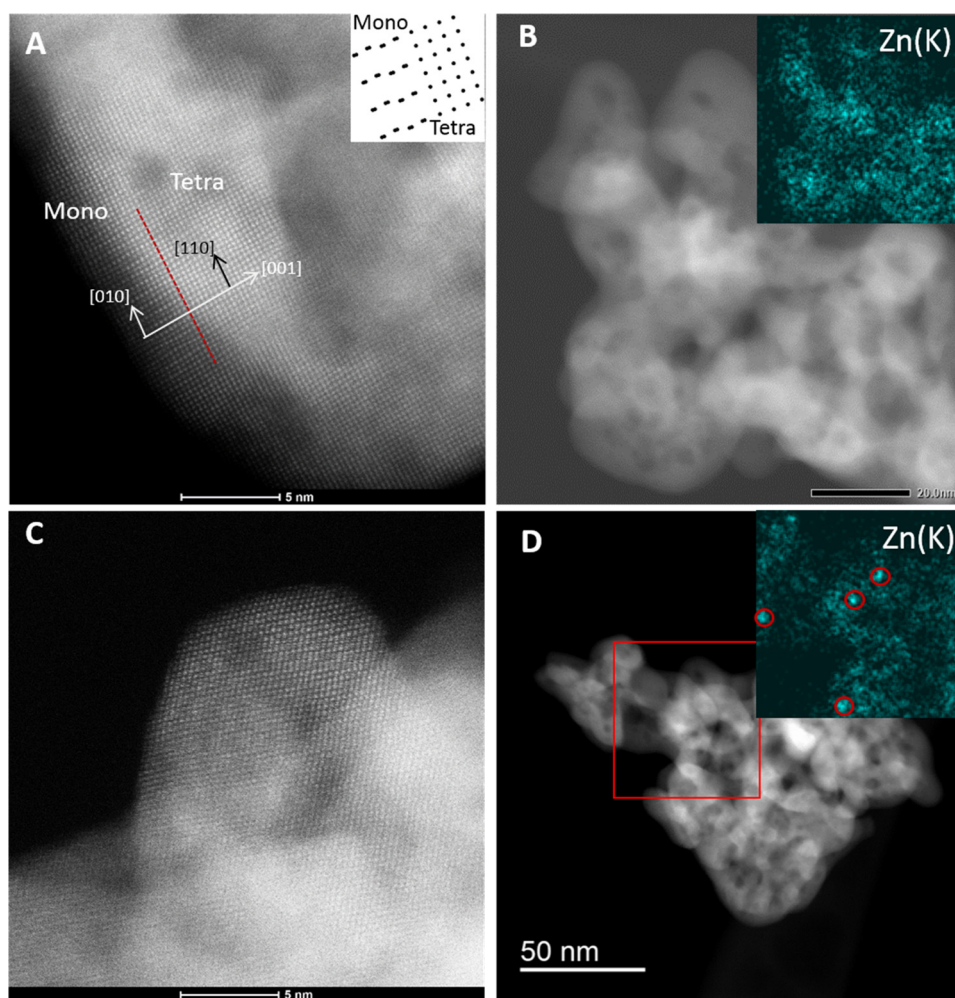**Fig. 3.** HAADF STEM images of one representative particle of (A) $Zn_1Zr_{10}O_z$ (inset represents an overlay detailing the coexisting t-ZrO_2 and m-ZrO_2 phases sharing a common (001) epitaxy) and (C) $Zn_1Zr_5O_z$. TEM images and corresponding Zn (K) elemental mapping (inset) of (B) $Zn_1Zr_{10}O_z$ and (D) $Zn_1Zr_5O_z$.
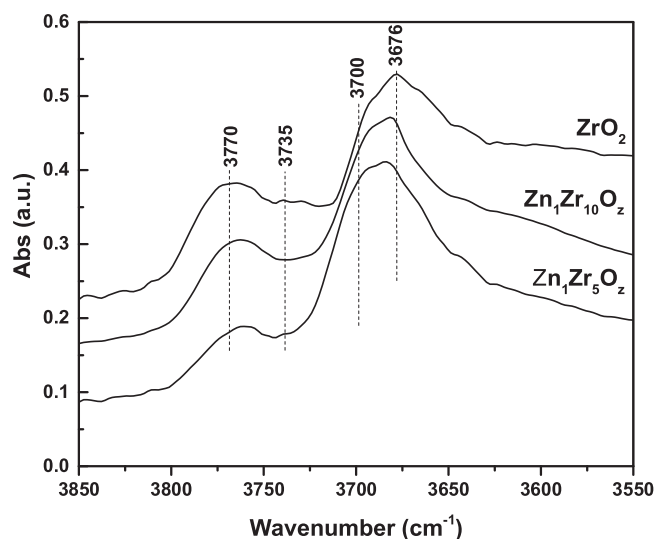

Fig. 4. IR spectra of hydroxyl groups on bulk ZrO_2 and $Zn_xZr_yO_z$ catalysts.

small amount of Brønsted acid sites on its surface, and that only Lewis acid sites are detected on $Zn_1Zr_{10}O_z$. Consistent with this observation, when the Zn/Zr ratio is finely adjusted from 1/60 to 1/20 (not shown), Lewis acid sites are always primarily observed, as evidenced by their corresponding peaks at 1607 and 1445 cm^{-1}. The minor peak at

1540 cm^{-1}, corresponding to Py adsorbed on Brønsted acid sites, decreases with increasing Zn/Zr ratio. In addition, both peaks at 1607 and 1445 cm^{-1}, characteristic of Py adsorbed on Lewis acid sites, experience a blue shift as Zn content is increased. This indicates that the surface Lewis acidity of the $Zn_xZr_yO_z$ catalysts is weakened after the incorporation of framework Zn^{2+} to the catalyst structure [47,67].

NH$_3$-TPD (Figure S3) was used to further quantify the acidic sites on the $Zn_xZr_yO_z$ catalysts with varying Zn/Zr ratios. Finke et al. has proposed that NH$_3$ adsorbs onto ZrO_2 in four forms: on terminal surface hydroxyl groups, on bridged surface hydroxyl groups, and on two different types of Zr^{4+} [68]. Numerical modelling has shown that the hydroxyl groups are weaker than the Zr^{4+} acidic sites from an estimation of desorption reaction activation energies. Based on this, we have deconvoluted four Gaussian peaks from the NH$_3$-TPD profiles for the $Zn_xZr_yO_z$ catalysts. The results are summarized in Table S2, and plotted in Fig. 6. As Zn/Zr ratio in the catalysts is increased, the density of stronger acidic sites decreases monotonically from 11.0×10^{-4} on ZrO_2 to 3.0×10^{-4} mmol/m^2 on $Zn_1Zr_{10}O_z$, consistent with what was observed in the Py-IR results. At the same time the density of medium acidic sites increases from 3.2×10^{-4} to 5.7×10^{-4} mmol/m^2 as Zn content increases in the catalysts. Regarding the weak acidic sites associated with hydroxyl groups, little or no change is observed between catalysts with differing Zn/Zr ratios (Table S2).

CO$_2$ was used as a probe molecule for investigation of basic sites on the surface of the $Zn_xZr_yO_z$ catalysts. CO$_2$-TPD was used to quantify the surface basicity of the catalysts (Figure S6–S7). Unfortunately, the
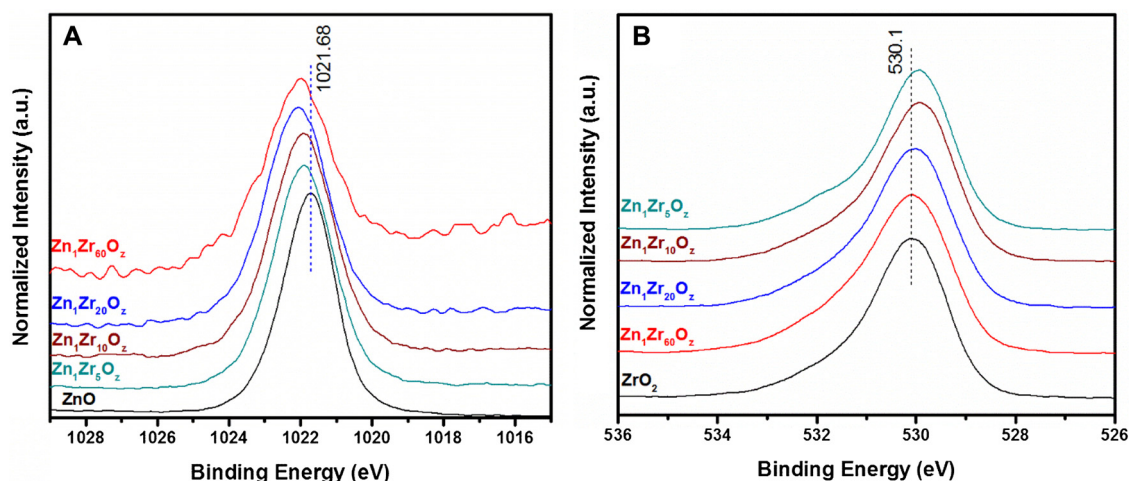
Fig. 5. XPS spectra of Zn $2p_{3/2}$ (A) and O 1s (B) regions of the $Zn_xZr_yO_z$ catalysts studied.

Table 1
Comparison of measured and hypothetical Zn/Zr ratios.

Catalysts	Ideal Zn/Zr ratio[1]	Measured surface Zn/Zr ratio[2]	Hypothetical surface Zn/Zr ratio[3]	Hypothetical Shell thickness[4] (nm)
$Zn_1Zr_5O_z$	0.20	0.41	5.85	2.0
$Zn_1Zr_{10}O_z$	0.10	0.25	2.92	1.5
$Zn_1Zr_{20}O_z$	0.05	0.14	1.46	1.4
$Zn_1Zr_{60}O_z$	0.02	0.04	0.49	1.5

Note: (1) total Zn/Zr ratio based on content used in synthesis; (2) the Zn/Zr ratio observed from XPS measurements; (3) the hypothetical surface Zn/Zr ratio was calculated by assuming all of the added Zn stays on the surface spherical catalyst particles of 20 nm in diameter and that the surface consists of stable monoclinic ZrO_2 (111) terminal structures; (4) This shell thickness calculation is based on the assumption that the catalyst is a spherical particle consisting of the t-ZrO2 phase (where the unit cell volume = 0.0691 nm^3 and one unit cell has 4 O and 2 Zr atoms).
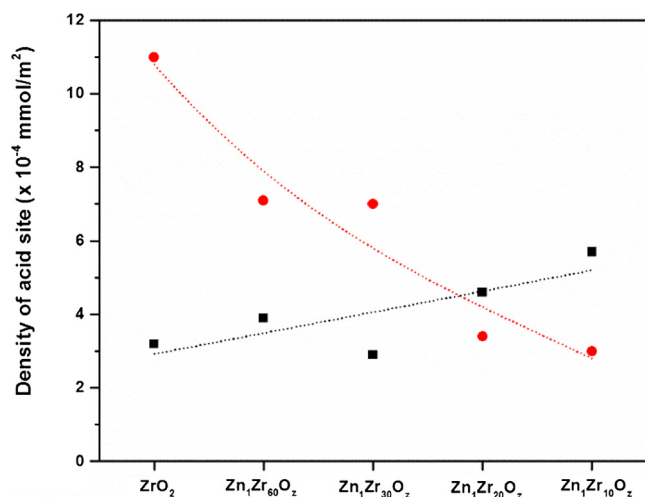

Fig. 6. Evolution of surface acid site density as a function of Zn/Zr ratio. Red corresponds to strong acid sites and black corresponds to medium strength acid sites (For interpretation of the references to colour in this figure legend, the reader is referred to the web version of this article).

density of all basic sites quantified by CO_2-TPD only show marginal changes with the Zn/Zr ratio over the range studied (Table S3). FTIR has been widely used in other works to monitor the different carbonate species (e.g., hydrogen carbonate, monodentate, bidentate and polydentate species) that correspond to basic sites with different strengths on the catalyst surface [65]. Fig. 7 shows the different carbonate species observed on the $Zn_xZr_yO_z$ catalysts at 50 and 300 °C. Spectra corresponding to different desorption temperatures (25, 50, 100, 200, 300, and 400 °C) on each sample are shown in Figure S5. Upon CO_2 adsorption followed by desorption at 50 °C (Fig. 7 A), the major bands on ZrO_2 are at 1626, 1575, 1431, and 1324 cm^{-1}. As Zn is added, bands at 1597, 1525, 1453, 1410, and 1360 cm^{-1} appear or increase in intensity when compared to bulk ZrO_2. The peak at 1225 cm^{-1} decreases with increasing Zn/Zr ratio. The bands at 1626 (asymmetric CO stretching), 1431 (symmetric CO stretching), and 1225 (OH bending) cm^{-1} are associated with hydrogen carbonate, formed by adsorption of CO_2 on basic hydroxyl groups. Their intensities decrease as Zn content (i.e., Zn/Zr ratio in the catalyst) is increased, indicating that the addition of Zn lowers the population of basic hydroxyl groups on the catalyst surface. The bands at 1575 and 1324 cm^{-1} associated with bidentate species slightly decrease with increasing Zn content (more noticeably at 1324 cm^{-1}). The bands at 1453 and 1410 cm^{-1} start appearing on $Zn_1Zr_{30}O_z$ and increase in intensity as Zn content is further increased. These bands were assigned to polydentate species [65]. The formation of bidentate and polydentate species is due to the interaction of CO_2 with Lewis acid-base pairs (Zr–O-Zr) and closely spaced coordinatively unsaturated (cus) cationic centers ($Zr^{\delta+}$), respectively. [65]. New bands at 1597, 1525, and 1360 cm^{-1} appear as well and increase with increasing Zn content. The new bands at 1525 and 1360 cm^{-1} can be attributed to bidentate carbonate species on the new Lewis acid-base pairs (Zr–O–Zn), and those at 1453 and 1360 cm^{-1} to polydentate ones on the new cus centers in close interaction with Zn. The bands at 1597 cm^{-1} is likely due to the new hydrogen carbonate species. These results are consistent from those from Raman spectra, and suggest that atomically dispersed Zn^{2+} is incorporated into the ZrO_2 framework, generating new surface Lewis acid-base pairs (i.e., Zr–O–Zn) and cus centers that are evidenced by the new adsorbed bidentate and polydentate species on the catalyst surface [53,69].

As desorption temperature increases, weakly adsorbed hydrogen carbonate bands decrease rapidly and disappear after 200 °C on all the $Zn_xZr_yO_z$ catalysts studied (Figure S5), leaving only strongly adsorbed bidentate and polydentate species with slight peak shift on the surface of the catalysts. Fig. 7B compares the spectra of the samples at a desorption temperature of 300 °C. After desorption at this temperature, the peak intensities of new bidentates (1531, 1360 cm^{-1}) and polydentate carbonate (1450 and 1431 cm^{-1}) increase with increasing Zn/Zr ratio, suggesting that the addition of Zn improves the strength of the surface basicity on the $Zn_xZr_yO_z$ catalysts, particularly basicity of the bridged O of Zn-O-Zr moiety.
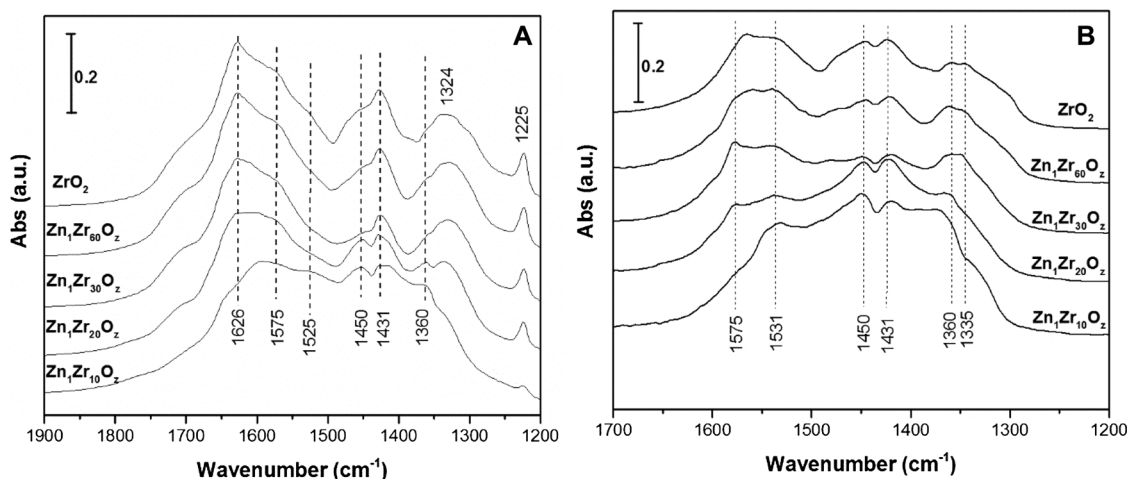
Fig. 7. CO$_2$-IR spectra of Zn$_x$Zr$_y$O$_z$ catalysts at desorption temperatures of 50 °C (A) and 300 °C (B).

3.2. Effect of Zn/Zr ratio on mixed MEK/acetone reactions

We recently reported that the mixed-metal oxide catalyst Zn$_1$Zr$_{10}$O$_z$ is highly selective and stable for the conversion of mixed carboxylic acid feeds (e.g., acetic acid and propionic acid) to produce a range of C$_3$-C$_6$ olefins, which likely proceeds via the self- and cross-ketonization of carboxylic acid followed by secondary self- and cross-aldolization of the mixed ketone intermediates [25]. Given the different electronic and acid-base properties induced by varying Zn/Zr ratios, we further studied the effect of Zn/Zr molar ratio on the self- and cross-condensation reactions involved in the mixed carboxylic acid to olefin conversion. Due to the complication of the multi-step cascade reactions, the current investigations are mainly focused on the rate determining mixed acetone and MEK reactions. Even with this mixed ketone reaction, the reactions involve a complex reaction network including both self-aldolization and cross-aldolization pathways. Fig. S8 proposed all the possible aldolization reaction paths for the mixed acetone and MEK reactions. From the product point of view, both self-aldolization and cross-aldolization could lead to the formation of C4 and C5 olefins. However, C6 olefins are only generated from cross-aldolization, which could be used to indicate the contribution of cross-aldolization in the mixed ketone reactions.

Prior to the experiments comparing the effects of Zn/Zr ratio on Zn$_x$Zr$_y$O$_z$ catalysts, a separate set of experiments on varying MEK and acetone feed ratio (MEK/acetone) over Zn$_1$Zr$_{20}$O$_z$ (Fig. S9) were carried out. The data from these experiments suggest that an MEK/acetone molar ratio of 2 gave the highest total yield to C$_4$-C$_6$ olefins. An MEK/acetone ratio of 2 was thus chosen to study the effect of Zn/Zr molar ratio on the (cross-) aldolization reactions as shown in Fig. 8. In general, complete acetone conversion was observed on all the catalysts studies. Fig. 8A and B show the effect of Zn/Zr ratio on MEK conversion and products distribution, respectively. Over ZrO$_2$, MEK conversion was low at 62.0%, and carbon balance is only 85% (Fig. 8B, inset). The C$_4$- C$_6$ olefin selectivity was only 15.0%, and decomposition reaction (Eqs. (1)–(3)) was found to dominate as evidenced by the high selectivity to methane and 3-pentanone. This observation is consistent with the acetone reactions on ZrO$_2$, on which decomposition products such as methane and CO$_2$, as well as a low carbon balance was observed [24]. The fact that very low ethane selectivity was observed suggests that the cleavage of methyl carbonyl C−C bond is dominant in the MEK decomposition (Eq. (2)) rather than the one of ethyl carbonyl bond (Eq. (3)). Upon addition of a small amount of Zn (i.e., Zn$_1$Zr$_{60}$O$_z$), however, MEK conversion increases from 62.0% to 83.0%. Carbon balance was also improved by about 5% (Fig. 8B, inset). Notably, the selectivity to C$_4$-C$_6$ olefins increases magnificently up to 61.0% as a result of the largely inhibited decomposition products (i.e., methane and 3-
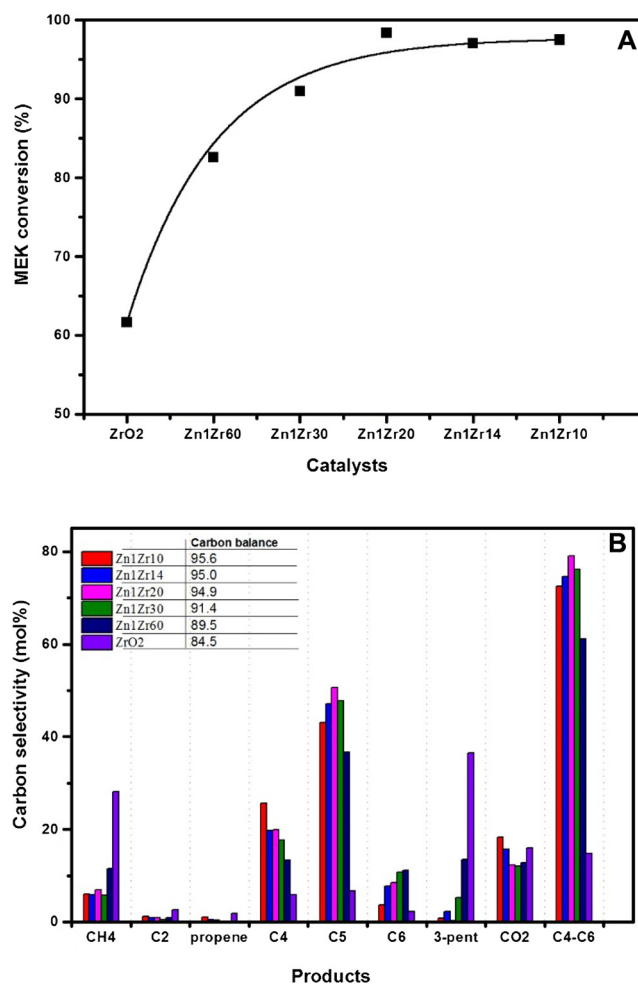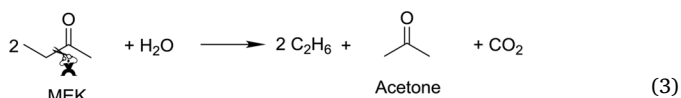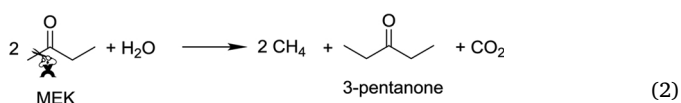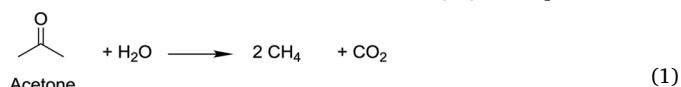

Fig. 8. MEK conversion (A) and Product distribution (B) in the mixed MEK/acetone reaction over Zn$_x$Zr$_y$O$_z$ catalysts. *400 mg catalyst, T = 415 °C, P$_{MEK}$ = 0.29 mol%, P$_{acetone}$ = 0.14 mol % S/C = 5, WHSV = 0.049 g$_{ketone}$ g$_{catal}$$^{-1}$ h^{-1}.*

pentanone). As the Zn/Zr ratio increases, both MEK conversion (Fig. 8A) and carbon balance (Fig. 8B, inset) increase monotonically. At the same time selectivity to C$_4$-C$_6$ olefins first increases and reaches a maximum at ∼80 mol % on the Zn$_1$Zr$_{20}$O$_z$ catalyst. Further increasing the Zn/Zr ratio leads to a slight increase of CO$_2$ selectivity at the

expense of C_4-C_6 olefins with methane selectivity remaining essentially constant. This observation indicates that steam reforming is slightly enhanced at higher Zn/Zr ratio, likely due to the formation of ZnO clusters as evidenced by STEM (Fig. 3) and Raman (Fig. 2) observations. Indeed, it has been reported that ZnO showed low activity in ethanol steam reforming reactions [24]. For individual olefins (Fig. 8B), as the Zn/Zr ratio increases (except for ZrO_2), carbon selectivity to C_4 olefins increases and that to C_6 decreases monotonically. The carbon selectivity to C_5 olefins reaches a maximum of 50.0 mol % at a Zn/Zr ratio of 1/20. When the Zn/Zr ratio is higher than 1/20, selectivity to C_4 olefins increases at the expense of C_5 and C_6 olefins. As abovementioned, while C_4 and C_5 olefins could be produced from both self- and cross-aldolization reactions, the C_6 olefins are exclusively from cross-aldolization reaction (Figure S8). The fact that selectivity to C_6 olefins decreases with Zn/Zr ratio suggests an inhibited cross-aldolization occurs at higher zinc content (i.e., higher Zn/Zr ratio). It should also be noted that, when the Zn/Zr ratio is less than 1/20, selectivity to C_4–C_6 olefins increases at the expense of decomposition products with Zn/Zr ratio. This improvement of C_4-C_6 olefin is mainly due to inhibited ketone decomposition (Eqs. (1)–(3))). Notwithstanding the observation of complicated self- and cross-condensation as well as secondary reactions, we confirmed that the mixed ketone reactions are very sensitive to the acid-base properties of the catalysts. A dedicated control of acid-base properties via Zn/Zr ratio is pivotal to not only inhibit side reactions (i.e., ketone decomposition, coke and oxidation) but the cross-aldolization reactions, and thus maximized C_4-C_6 olefin production.

$$\text{Acetone} + H_2O \longrightarrow 2\,CH_4 + CO_2 \qquad (1)$$

$$2\,\text{MEK} + H_2O \longrightarrow 2\,CH_4 + \text{3-pentanone} + CO_2 \qquad (2)$$

$$2\,\text{MEK} + H_2O \longrightarrow 2\,C_2H_6 + \text{Acetone} + CO_2 \qquad (3)$$

To summarize this part, the addition of a suitable amount of Zn not only improves carbon balance by inhibiting side reactions such as ketone decomposition and coking, but also enhances the ketone aldolization reactivity (Fig. 8). Most importantly, the Zn/Zr ratio of the $Zn_xZr_yO_z$ catalyst shows a significant effect on self- and cross-aldolization of ketone in the reaction pathway, and thus greatly affects the distribution of light olefins produced. A high carbon yield up to ~80.0 mol % to C_4-C_6 olefins can be achieved using a feed ratio of MEK/acetone = 2 on $Zn_1Zr_{20}O_z$.

4. Discussion

Depending on the size, valence, pretreatment temperature, and content of the dopants, the phase of the doped ZrO_2 can vary [58,60,61,63]. In this work on $Zn_xZr_yO_z$ catalysts our XRD, STEM, Raman, XPS, and FTIR analyses reveal that the incorporation of Zn^{2+} leads exclusively to the formation of tetragonal ZrO_2 after calcination at 550 °C for 3 h, which is consistent with what has previously been reported in literature [60]. In addition, it was found that, when the Zn/Zr ratio is lower than 1/10, the Zn^{2+} is atomically distributed within a thin outer shell (1.5–2.0 nm) of the catalyst particles. When the Zn/Zr ratio is above 1/10, ZnO clusters were detected that coexist with atomically dispersed Zn^{2+} (Figs. 2 and 3). It is notable that, despite the stabilized bulk tetragonal phase of the catalyst, the surface chemistry of the $Zn_xZr_yO_z$ catalysts are similar to that of monoclinic ZrO_2, as evidenced by the pattern of the hydroxyl groups observed in this work (Fig. 4). Patches of surface monoclinic phase on the surface are also seen in STEM images of the samples (Fig. 3). Similar structures were

also proposed ZrO_2 doped with other elements such as S and Y [62].

More importantly, results from Raman spectra, STEM, and XPS data suggest that the incorporation of Zn into the ZrO_2 promotes the formation of new Lewis acid-base active structure (i.e., Zr-O-Zn) on the catalyst surface. The observed acid-base properties of the catalysts studied were further confirmed by our Py-IR, CO_2-IR, NH_3-TPD, and CO_2-TPD results. These properties are believed to be pivotal to the activity of the cascade aldolization and self-deoxygenation reactions that take place on the catalyst [47]. NH_3-TPD results reveal that the incorporation of Zn significantly decreases the density of strong acidic sites from 11.0×10^{-4} mmol/m^2 on ZrO_2 to 3.0×10^{-4} mmol/m^2 on $Zn_1Zr_{10}O_z$, and increases the density of medium acidic sites from 3.2×10^{-4} mmol/m^2 on ZrO_2 to 5.7×10^{-4} mmol/m^2 on $Zn_1Zr_{10}O_z$ (Fig. 6). The passivation of strong acid sites on ZrO_2 could be related to the inhibition of side reactions to methane/coke and thus improved olefin selectivity/carbon balance on the $Zn_xZr_yO_z$ catalysts. Despite the fact that CO_2-TPD shows this passivation has only a marginal effect on surface basicity, CO_2-IR results reveal the formation of new surface Lewis acid-base pairs on $Zn_xZr_yO_z$ catalysts, as evidenced by the newly formed and increased bidentate and polydentate species (Fig. 7). These results are complemented through XPS spectra showing electron transfer from the framework Zn^{2+} to the neighboring O (Fig. 5). A comparison of the of molar ratio of acid-to-base surface sites derived from NH_3/CO_2-TPD (Fig. 9) shows that the number of strong acid sites become less as catalyst Zn content is increased, providing further confirmation that Zn addition contributes to the passivation of strong acid sites on the catalyst surface. Notably, in spite of the increased density of medium acid site, the ratio of medium acid and medium base initially increases with the addition of Zn before reaching a constant value near one with continued addition. Based on the proposed stability of surface carbonates in literature [65], we propose that these medium sites identified by NH_3-TPD and CO_2-TPD are newly generated Lewis acid-base active site pairs (i.e, Zr–O–Zn).

The sites identified by strongly adsorbed CO_2 could represent closely spaced cus (coordinately unsaturated sites) cationic sites (or oxygen vacancies). The incorporation of Zn into the framework of ZrO_2 promotes the formation of oxygen vacancies, and thus cus cationic centers. The enhanced formation of oxygen vacancies was additionally confirmed in our IR experiments, as evidenced by increasing band intensity at 3700 cm^{-1} (Fig. 3) representative of hydroxyl groups in proximity to oxygen vacancies [66] as catalyst Zn content was increased. Enhanced formation of oxygen vacancies on $Zn_xZr_yO_z$ has also been observed by other groups [56,69]. Surface oxygen vacancy on
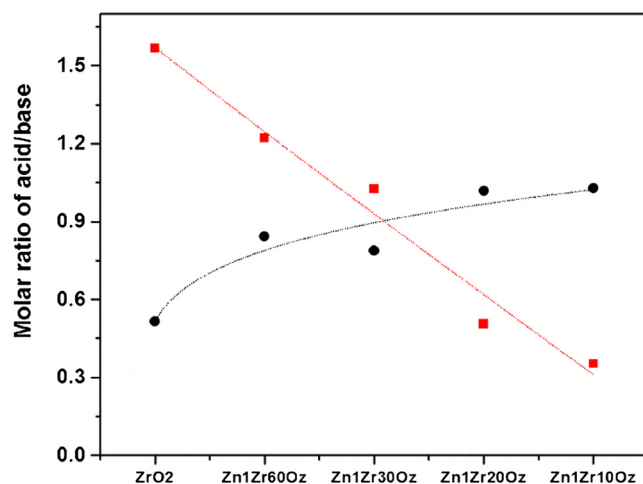

Fig. 9. Comparison of acid-to-base molar ratio on the surface the $Zn_xZr_yO_z$ catalysts studied. Red corresponds to strong acid sites and black corresponds to medium strength acid sites (For interpretation of the references to colour in this figure legend, the reader is referred to the web version of this article).

metal oxides has been shown to be crucial in stabilization and activation of aldehyde for C—C coupling (aldol-condensation) reactions [56,70,71]. In the current cascade aldolization and self-deoxygenation reactions, we hypothesize that the enhanced formation of oxygen vacancy could be essential to the (cross) aldolization. However, it is still yet unclear whether those cus centers will play a role in the self-deoxygenation rate-determining step [72] or not, which is subject to further studies.

We have shown that acetone to isobutene reaction is very sensitive to the acid-base properties on the $Zn_xZr_yO_z$ catalysts, leading to either acetone decomposition as a side reaction or the main cascade aldolization reaction pathway [25]. For the mixed ketone reactions, the acid-base properties showed clear influence on the cross-condensation activity, as evidenced by the varied Zn/Zr ratio experiments (Fig. 8 & Section 3.2). When Zn/Zr molar ratios of the catalysts increase from 0 to 1/20, the surface acid-base site pairs in ZrO_2 (i.e., Zr–O–Zr) are gradually replaced by the newly generated Lewis acid-base pairs (i.e., Zr–O–Zn) that are highly active and selective for cascade ketone aldolization and self-deoxygenation reactions. Indeed, the strong acid sites on ZrO_2 (i.e., Zr–O–Zr) decrease rapidly, and medium one (proposed as Zr–O–Zn) increase (Fig. 7). An increase in selectivity to the major C_4-C_6 olefins products at the expense of side products (methane, ethane, and 3-pentanone) further confirms our hypothesis that the new Zr-O-Zn acid-base pairs are active sites for the cascade aldolization and self-deoxygenation reactions (section 3.2). When the catalyst Zn/Zr ratio surpass 1/20, the selectivity to CO_2 start increasing at the expense of C_4-C_6 olefins, indicative of steam reforming side reactions. The occurrence of steam reforming reactions after Zn/Zr ratio of 1/20 suggest that majority of the surface acid-base site pairs (Zr–O–Zr) on ZrO_2 have been replaced by the new Lewis acid-base site pairs (Zr–O–Zn) at Zn/Zr = 20 (i.e., $Zn_1Zr_{20}O_z$), above which Zn–O–Zn or ZnO clusters appear and increases with Zn/Zr ratio. This hypothesis matches well with the Raman and STEM observations though the ZnO clusters only becomes observable at Zn/Zr ratio > 1/10 (i.e., $Zn_1Zr_5O_z$). In addition, the achievement of a relatively constant ratio of medium acid to medium base sites after Zn/Zr = 20 (Fig. 9) also confirms the completion of replacement of Zr-O-Zr by Zr-O-Zn new site pairs. The steam reforming reaction on ZnO has been previously observed by both our group [25] and others [73].

More importantly, individual olefin changes with Zn/Zr ratio. As Zn/Zr ratio increases from 1/60 to 1/10, isobutene continues to increase and C_6 olefins decreases. The selectivity to C_5 olefins first increase and then decreases, peaking at the Zn/Zr of 1/20. Given that C_6 olefins are exclusively from cross-aldolization pathway (Fig. S8), the decreasing C_6 selectivity with Zn/Zr ratio suggests that, other than the inhibition of side decomposition reactions, the acid-base properties of the surface also influence the cross-aldolization reactivity of the catalyst. The favorable cross-aldolization at lower Zn content (i.e. lower Zn/Zr ratio) is still not fully understood. However, it is hypothesized that, although the medium Lewis acid-base site pairs are essential to inhibiting the decomposition side reactions and thus the enhanced major aldolization pathway, the co-existence of some strong acid sites might affect adsorption of reactants and products to favor cross-aldolization reactions and thus the final distribution of C_4-C_6 olefins.

5. Conclusions

Mixtures of ketone and carboxylic acids are commonly found in fermentation products and a mean to their direct conversion to value-added fuels/chemicals is highly desirable as an alternative to fossil based processes. Over $Zn_xZr_yO_z$ catalysts we observed and confirmed that mixed ketones (acetone and MEK) undergo self- and cross-aldolization and self-deoxygenation to yield C_4-C_6 olefins. Most importantly, our results unambiguously show that the formation of atomically dispersed Zn^{2+} in the ZrO_2 framework not only passivates the strong Lewis acid sites existing on bulk ZrO_2, but more importantly generate new

surface Lewis acid-base site pairs (i.e., Zr–O–Zn) that are responsible for cascade ketone-to-olefin conversion. An appropriate amount of Zn^{2+} (producing a Zn/Zr ratio of 1/30-1/10) is required to replace the acid-base site pairs on ZrO_2 (i.e., Zr–O–Zr) while minimizing the formation of ZnO phase (i.e., Zn–O–Zn), which both lead to side reactions (i.e., decomposition of reactants on ZrO_2 and their oxidation to CO_2 on ZnO). While it is still unclear how the catalyst Zn/Zr ratio affects cross-condensation activities, the co-existence of a small portion of strong acid sites with newly formed Lewis acid-base site pairs seems to be pivotal in achieving the best cross-condensation products. The optimized catalyst for C_4-C_6 olefin production in this work was found to be $Zn_1Zr_{20}O_z$, achieving a carbon yield of ~80.0 mol % to C_4-C_6 olefins.

Appendix A. Supplementary data

Supplementary material related to this article can be found, in the online version, at doi:https://doi.org/10.1016/j.apcatb.2018.04.051.

References

[1] Y.-K. Park, C.W. Lee, N.Y. Kang, W.C. Choi, S. Choi, S.H. Oh, D.S. Park, Catal. Surv. Asia 14 (2010) 75–84.
[2] H.M.T. Galvis, K.P. de Jong, Acs Catal. 3 (2013) 2130–2149.
[3] M. Janardanarao, Ind. Eng. Chem. Res. 29 (1990) 1735–1753.
[4] M. Zhang, Y. Yu, Ind. Eng. Chem. Res. 52 (2013) 9505–9514.
[5] S.P. Katikaneni, J.D. Adjaye, R.O. Idem, N.N. Bakhshi, Ind. Eng. Chem. Res. 35 (1996) 3332–3346.
[6] L.F. Albright, Ind. Eng. Chem. Res. 41 (2002) 5627–5631.
[7] A.C. Council, Product Stewardship Summary Higher Olefins Category, American Chemistry Council, 2008.
[8] H.M. Torres Galvis, K.P. de Jong, ACS Catal. 3 (2013) 2130–2149.
[9] P. Tian, Y. Wei, M. Ye, Z. Liu, ACS Catal. 5 (2015) 1922–1938.
[10] A.J. Ragauskas, C.K. Williams, B.H. Davison, G. Britovsek, J. Cairney, C.A. Eckert, W.J. Frederick, J.P. Hallett, D.J. Leak, C.L. Liotta, Science 311 (2006) 484–489.
[11] G.W. Huber, S. Iborra, A. Corma, Chem. Rev. 106 (2006) 4044–4098.
[12] C.J. Liu, H.M. Wang, A.M. Karim, J.M. Sun, Y. Wang, Chem. Soc. Rev. 43 (2014) 7594–7623.
[13] J.M. Sun, A.M. Karim, H. Zhang, L. Kovarik, X.H.S. Li, A.J. Hensley, J.S. McEwen, Y. Wang, J. Catal. 306 (2013) 47–57.
[14] G.W. Huber, S. Iborra, A. Corma, Chem. Rev. 106 (2006) 4044–4098.
[15] H.L. Drake, A.S. Gößner, S.L. Daniel, Ann. N. Y. Acad. Sci. 1125 (2008) 100–128.
[16] S. Herrmann, E. Iglesia, J. Catal. 346 (2017) 134–153.
[17] S. Wang, E. Iglesia, J. Phys. Chem. C 120 (2016) 21589–21616.
[18] S. Wang, K. Goulas, E. Iglesia, J. Catal. 340 (2016) 302–320.
[19] J. Quesada, L. Faba, E. Díaz, S. Bennici, A. Auroux, S. Ordóñez, J. Catal. 329 (2015) 1–9.
[20] M. León, L. Faba, E. Díaz, S. Bennici, A. Vega, S. Ordóñez, A. Auroux, Appl. Catal. B 147 (2014) 796–804.
[21] J. Sun, Y. Wang, Acs Catal. 4 (2014) 1078–1090.
[22] M. Iwamoto, Catal. Today 242 (2015) 243–248.
[23] A.G. Gayubo, A.T. Aguayo, A. Atutxa, R. Aguado, J. Bilbao, Ind. Eng. Chem. Res. 43 (2004) 2610–2618.
[24] R.A. Baylon, J. Sun, Y. Wang, Catal. Today 259 (2016) 446–452.
[25] R.A. Baylon, J. Sun, K.J. Martin, P. Venkitasubramanian, Y. Wang, Chem. Commun. (Camb.) 52 (2016) 4975–4978.
[26] F. Polo-Garzon, S.Z. Yang, V. Fung, G.S. Foo, E.E. Bickel, M.F. Chisholm, D.E. Jiang, Z.L. Wu, Angew. Chem. Int. Ed. 56 (2017) 9820–9824.
[27] G.S. Foo, F. Polo-Garzon, V. Fung, D.E. Jiang, S.H. Overbury, Z.L. Wu, ACS Catal. 7 (2017) 4423–4434.
[28] T. Inoue, M. Itakura, H. Jon, Y. Oumi, A. Takahashi, T. Fujitani, T. Sano, Microporous Mesoporous Mater. 122 (2009) 149–154.
[29] J.F. Haw, W. Song, D.M. Marcus, J.B. Nicholas, Acc. Chem. Res. 36 (2003) 317–326.
[30] K.K. Ramasamy, H. Zhang, J. Sun, Y. Wang, Catal. Today 238 (2014) 103–110.
[31] T. Tago, H. Konno, S. Ikeda, S. Yamazaki, W. Ninomiya, Y. Nakasaka, T. Masuda, Catal. Today 164 (2011) 158–162.
[32] T. Tago, H. Konno, M. Sakamoto, Y. Nakasaka, T. Masuda, Appl. Catal. A 403 (2011) 183–191.
[33] A.G. Gayubo, A.T. Aguayo, A. Atutxa, R. Aguado, M. Olazar, J. Bilbao, Ind. Eng.

Chem. Res. 43 (2004) 2619–2626.

[34] T. Inoue, M. Itakura, H. Jon, Y. Oumi, A. Takahashi, T. Fujitani, T. Sano, Microporous Mesoporous Mater. 122 (2009) 149–154.

[35] U.V. Mentzel, S. Shunmugavel, S.L. Hruby, C.H. Christensen, M.S. Holm, J. Am. Chem. Soc. 131 (2009) 17009–17013.

[36] C.J. Liu, A.M. Karim, V.M. Lebarbier, D.H. Mei, Y. Wang, Top. Catal. 56 (2013) 1782–1789.

[37] R.W. Snell, B.H. Shanks, ACS Catal. 3 (2013) 783–789.

[38] G. Pacchioni, ACS Catal. 4 (2014) 2874–2888.

[39] T.N. Pham, T. Sooknoi, S.P. Crossley, D.E. Resasco, ACS Catal. 3 (2013) 2456–2473.

[40] A. Biaglow, J. Sepa, R. Gorte, D. White, J. Catal. 151 (1995) 373–384.

[41] C.A. Gaertner, J.C. Serrano-Ruiz, D.J. Braden, J.A. Dumesic, J. Catal. 266 (2009) 71–78.

[42] O. Nagashima, S. Sato, R. Takahashi, T. Sodesawa, J. Mol. Catal. A: Chem. 227 (2005) 231–239.

[43] V. Crocella, G. Cerrato, C. Morterra, Phys. Chem. Chem. Phys. 15 (2013) 13446–13461.

[44] R. King, H. Idriss, Langmuir 25 (2009) 4543–4555.

[45] V. Crocellà, C. Morterra, J. Phys. Chem. C 114 (2010) 18972–18987.

[46] C.J. Barrett, J.N. Chheda, G.W. Huber, J.A. Dumesic, Appl. Catal. B 66 (2006) 111–118.

[47] J. Sun, R.A. Baylon, C. Liu, D. Mei, K.J. Martin, P. Venkitasubramanian, Y. Wang, J. Am. Chem. Soc. 138 (2016) 507–517.

[48] C. Liu, J. Sun, C. Smith, Y. Wang, Appl. Catal. A 467 (2013) 91–97.

[49] J. Sun, K. Zhu, F. Gao, C. Wang, J. Liu, C.H. Peden, Y. Wang, J. Am. Chem. Soc. 133 (2011) 11096–11099.

[50] A.J. Crisci, H. Dou, T. Prasomsri, Y. Román-Leshkov, Acs Catal. 4 (2014) 4196–4200.

[51] V.L. Dagle, C. Smith, M. Flake, K.O. Albrecht, M.J. Gray, K.K. Ramasamy, R.A. Dagle, Green Chem. 18 (2016) 1880–1891.

[52] C. Smith, V.L. Dagle, M. Flake, K.K. Ramasamy, L. Kovarik, M. Bowden, T. Onfroy, R.A. Dagle, Catal. Sci. Technol. 6 (2016) 2325–2336.

[53] C.Y. Wang, G. Garbarino, L.F. Allard, F. Wilson, G. Busca, M. Flytzani-Stephanopoulos, Acs Catal. 6 (2016) 210–218.

[54] J. Sun, C. Liu, Y. Wang, K. Martin, P. Venkitasubramanian, Process and catalyst for conversion of acetic acid to isobutene, US Patent 9,586,194, 2017.

[55] J. Sun, C. Liu, Y. Wang, K. Martin, P. Venkitasubramanian, Process and catalyst for conversion of acetic acid to isobutene and propylene, US Patent 9,580,365, 2017.

[56] Ld.R. Silva-Calpa, P.C. Zonetti, C.P. Rodrigues, O.C. Alves, L.G. Appel, R.R. de Avillez, J. Mol. Catal. A: Chem. 425 (2016) 166–173.

[57] F. Liu, Y. Men, J.G. Wang, X.X. Huang, Y.Q. Wang, W. An, ChemCatChem 9 (2017) 1758–1764.

[58] V.G. Keramidas, W.B. White, J. Am. Ceram. Soc. 57 (1974) 22–24.

[59] J. Joo, T. Yu, Y.W. Kim, H.M. Park, F. Wu, J.Z. Zhang, T. Hyeon, J. Am. Chem. Soc. 125 (2003) 6553–6557.

[60] G. Štefanić, S. Musić, M. Ivanda, J. Mol. Struct. 924 (2009) 225–234.

[61] G. Stefanic, M. Didovic, S. Music, J. Mol. Struct. 834 (2007) 435–444.

[62] M. Li, Z. Feng, G. Xiong, P. Ying, Q. Xin, C. Li, J. Phys. Chem. B 105 (2001) 8107–8111.

[63] C. Li, M. Li, J. Raman Spectrosc. 33 (2002) 301–308.

[64] S. Karlin, P. Colomban, J. Am. Ceram. Soc. 82 (1999) 735–741.

[65] B. Bachiller-Baeza, I. Rodriguez-Ramos, A. Guerrero-Ruiz, Langmuir 14 (1998) 3556–3564.

[66] A. Badri, C. Binet, J.-C. Lavalley, J. Chem. Soc., Faraday Trans. 92 (1996) 4669–4673.

[67] B.H. Davis, R.A. Keogh, S. Alerasool, D.J. Zalewski, D.E. Day, P.K. Doolin, J. Catal. 183 (1999) 45–52.

[68] T. Finke, M. Gernsbeck, U. Eisele, C. Vincent, M. Hartmann, S. Kureti, H. Bockhorn, Thermochim. Acta 473 (2008) 32–39.

[69] C.Y. Wang, M. Boucher, M. Yang, H. Saltsburg, M. Flytzani-Stephanopoulos, Appl. Catal., B 154 (2014) 142–152.

[70] F.C. Calaza, Y. Xu, D.R. Mullins, S.H. Overbury, J. Am. Chem. Soc. 134 (2012) 18034–18045.

[71] A. Gangadharan, M. Shen, T. Sooknoi, D.E. Resasco, R.G. Mallinson, Appl. Catal. A 385 (2010) 80–91.

[72] J.M. Sun, R.A.L. Baylon, C.J. Liu, D.H. Mei, K.J. Martin, P. Venkitasubramanian, Y. Wang, J. Am. Chem. Soc. 138 (2016) 507–517.

[73] J. Llorca, P.R. de la Piscina, J. Sales, N. Homs, Chem. Commun. (2001) 641–642.